Large-eddy simulation of turbulent reacting flows

Heinz Pitsch [a,*], Olivier Desjardins [a], Guillaume Balarac [b], Matthias Ihme [c]

[a] Department of Mechanical Engineering, Stanford University, 488 Escondido Mall, Stanford, CA 94024, USA
[b] Center for Turbulence Research, USA
[c] Department of Aerospace Engineering, University of Michigan, Ann Arbor, MI 48109, USA

ABSTRACT

In this paper, a few advances and challenges towards predictive large-eddy simulations of turbulent reacting flow are discussed in the context of numerical simulations of aircraft engines, which require an adequate description of liquid fuel injection, liquid fuel atomization, drop breakup, drop dynamics, and evaporation, large-scale turbulent fuel air mixing, small scale molecular fuel air mixing, chemical reactions, and turbulence/chemistry interactions. We have identified three of the most important and most challenging modeling problems in this process, namely primary atomization, sub-filter scalar mixing, and pollutant formation. Some recent progress on all three topics is presented.

© 2008 Elsevier Ltd. All rights reserved.

Contents

1. Introduction

Numerical simulations of combustion in aircraft engines is quite complex, as it requires an adequate description of liquid fuel injection, liquid fuel atomization, drop breakup, drop dynamics, and evaporation, large-scale turbulent fuel air mixing, small scale molecular fuel air mixing, chemical reactions, and turbulence/chemistry interactions. Many of these processes happen on multiple time and length scales, which creates a modeling challenge. Turbulent combustion is a prime example for a multiscale problem, since turbulence at high Reynolds numbers obviously has a wide range of scale, but the range of chemical

* Corresponding author.
  E-mail address: h.pitsch@stanford.edu (H. Pitsch).

time scales that is involved, for example, in the formation of pollutants is even wider. The interaction of chemistry with turbulent and molecular mixing not only involves all of these scales, but creates additional scales that are related to the production and consumption layers of chemical species and sensible energy. These flame scales directly involve molecular mixing, since in non-premixed flames, combustion only takes place if fuel and air are mixed on a molecular level, or, in premixed flames, when fresh unburned gases are heated up sufficiently by heat conduction from the burned gases. Therefore, in turbulent combustion, where molecular transport occurs almost exclusively on the smallest turbulent scales, the combustion process happens on the small scales too.

In large-eddy simulations (LES), the large, energy containing turbulent motions are resolved and directly computed, and the small scale turbulent motions and their effect on the large scales has to be modeled. Because the combustion process occurs on the small scales of the turbulent motions, there is essentially no resolved part of the combustion process. Although the combustion process has to be modeled entirely, in the past, we have shown in many examples that LES provide much more accurate solutions for turbulent combustion problems than Reynolds-averaged Navier–Stokes (RANS) modeling approaches [1–3]. The reason is that, because of the turbulence cascade, the small scale turbulent motions and the small scale molecular mixing process are very much governed by the large scales of the turbulence, which, using LES, is typically captured with good accuracy. Pitsch [2] showed for the example of a piloted jet flame that the consideration of fluctuations in the small scale mixing rate predicted by LES, strongly improved the predictions of stable intermediates, such as carbon monoxide. Apparently, rare events of very high scalar dissipation rate are suppressed in rich partially premixed regions of the flame. Raman and Pitsch [3] performed LES of a bluff-body stabilized flame and demonstrated very good predictions of species mass fractions and temperature, which had not been achieved with any RANS-based approach. The analysis showed that the thin shear layers downstream of the bluff-body edge undergo Kelvin–Helmholtz instabilities and break down approximately one bluff-body diameter downstream of the nozzle. However, very rarely, this breakdown occurs right at the edge of the bluff body and a large amount of air is entrained into the otherwise rich interior of the recirculation region just downstream of the bluff body. These infrequent events change the dynamics of the flame, and it is obvious that such events cannot be predicted by Reynolds-averaged methods. Both these examples have in common that a highly non-linear process, in this case the turbulent combustion process involving the turbulence, the chemistry, and their interactions, is affected by rare infrequent events; and for strongly non-linear processes, even very rare events can change the first-order dynamics of the problem.

Several other phenomena of more practical relevance can be found in gas turbine engines that share these characteristics. As an example, in aircraft engines, the primary atomization process of the liquid fuel typically occurs because of high shear between the liquid and gaseous phase, for instance, in liquid sheets or liquid jets in crossflow. Even if most of the liquid phase first breaks up into larger lumps of liquid, which will then undergo breakup to smaller and smaller sizes, there might be a few very small droplets sheared off the liquid sheet or jet. Although only a very small percentage of the mass will be in these droplets, they evaporate very fast and can potentially provide the fuel that dominates the flame stabilization process.

Another example is the formation of soot in aircraft engines. Soot is formed in rich regions where the equivalence ratio is larger than about two. These rich regions typically exist in the primary combustion region, where as a consequence, large amounts of soot are usually formed. These regions form a sharp interface with the leaner regions, because of fast oxidation reactions mainly with OH. Further downstream, because of the introduction of secondary air, the equivalence ratio decreases, and most of the soot burns off. However, on rare occasions, a rich pocket survives the secondary mixing region, which brings a large amount of soot into the exhaust. It could be speculated that a large fraction of particulate emissions from aircraft engines come from very few rich pockets with high soot volume fraction rather than from the bulk of the fluid.

In the present paper, we will discuss some recent progress on a few of the topics listed above as being particularly relevant in aircraft engine combustion. We will start by discussing the primary atomization process, and in particular, describe numerical algorithms that can be used in LES of high-shear atomization. These algorithms will be applied here in direct numerical simulations that are performed to develop sub-filter models for LES. Next, we will discuss new accurate models for LES describing the sub-filter scalar mixing process. Mixing of fuel and air is described in terms of the mixture fraction, which provides a measure for the local equivalence ratio. Here, sub-filter models for the variance of the mixture fraction, will be presented. Finally, a model for the formation of oxides of nitrogen, NO_x, for turbulent combustion will be developed, and an application of the model in LES of an aircraft engine combustor will be presented. More information on the presented material can be found in Desjardins et al. [4], Balarac et al. [5], and Ihme and Pitsch [6].

2. Modeling primary atomization in aircraft engines

In most combustion devices it is desirable to achieve the fuel atomization and evaporation process as fast as possible. To promote instabilities and the highest possible impact of the low density air, fuel is typically injected through nozzles that are small compared with the scales of the device, resulting in thin sheets or jets. In addition, high shear between liquid fuel and air is produced either by high pressure injection, such as in diesel engines, or through high air velocity. These techniques produce a large variety of scales, ranging from the height of the air channels and the related large turbulent length scales over the characteristic size of the nozzle to the small droplets produced in the high shear regions. This range of scales, and in addition, the high density ratio that is typically encountered, make it extremely difficult to model the primary atomization process. The turbulent atomization of a liquid jet is a good example to summarize the challenges: the density ratio between the liquid and the gas is large, liquid mass conservation is paramount, and the competing physical processes lead to the formation of extremely thin liquid structures. These thin liquid structures are complex to resolve, and they carry a lot of momentum and have a strong influence on the turbulence.

Therefore, numerical schemes are required that are capable of tracking the liquid–gas interface at the limit of the numerical resolution, with high density ratios, while maintaining good conservation properties. In this section, we will describe a new numerical algorithm by Desjardins et al. [4] that satisfies these properties. The numerical scheme is intended for use in LES and DNS. The method will here be applied in DNS of a liquid jet, which is performed to develop sub-filter models for the application in LES.

Different methods have been proposed in the past for numerical simulations of interfacial flows. Level set methods are attractive, since the interface is described by a smooth function, which has many advantages. However, level set methods do not inherently conserve the volume of different phases, which is

critical in reacting flow simulations. Recently, Olsson and Kreiss [7] proposed a conservative level set (CLS) method that can strongly reduce the problem of mass conservation with no additional cost compared to standard schemes. This approach is improved here by introducing the accurate CLS (ACLS) method, which increases accuracy and robustness through the use of an additional distance level set as well as high order numerical techniques. This novel methodology provides a low-cost alternative to the hybrid level set methods such as the particle level set (PLS) method by Enright et al. [8] or the coupled level set method/volume of fluid technique (CLSVOF) by Sussman and Puckett [9].

However, the proposed CLS technique by itself would rely on a smeared-out density jump as well as on spread-out delta functions to represent the interfacial forces. This would lead to a less accurate representation of the front instabilities and to a less robust formulation prone to numerical instabilities such as spurious currents. In order to greatly reduce these issues, the ACLS method is combined with the ghost fluid method (GFM) [10,11], which treats the front as a sharp discontinuity, explicitly adding jump conditions to represent the surface tension force and the density jump across the interface. Combining the ACLS approach with the GFM provides a low-cost and scalable level set method that has good mass conservation properties and retains a sharp description of the front. Such a method becomes therefore applicable in more complex geometries, and remains tractable for large scale problems, such as the DNS of an atomizing liquid jet. This approach is likely to be very useful also for other interfacial flows, such as sheet and vortex cavitation, and the simulation of free-surface flows, e.g. around ship hulls. The details of the combined ACLS/GFM method are omitted here, but an extensive description of the method can be found in Desjardins et al. [4].

2.1. Accurate conservative level set (ACLS)

2.1.1. Hyperbolic tangent level set

In level set methods, an interface is defined as an iso-surface at a given value of the so-called level set function, which is typically chosen to be a smoothly varying scalar field variable. The definition of the level set function away from the interface value is arbitrary within certain constraints, but the most common definition of the level set function is that of a distance function, which will be denoted here by ϕ. This definition has the advantage that the level set function varies smoothly through the interface. The problem is that, as mentioned earlier, the mass on each side of the interface is not conserved. Instead of a signed distance function, Olsson and Kreiss [7,12] employed a hyperbolic tangent function ψ defined as

$$\psi(\mathbf{x}, t) = \frac{1}{2}\left(\tanh\left(\frac{\phi(\mathbf{x}, t)}{2\varepsilon}\right) + 1\right), \tag{1}$$

where ε is a parameter that sets the thickness of the profile. Rather than defining the interface location by the iso-surface $\phi = 0$, it is now defined by the location of the $\psi = 0.5$ iso-surface. The transport of the interface can still be performed by solving the level set equation for ψ. However, it can also be written in conservative form provided the velocity field $\mathbf{u}$ is solenoidal, i.e. $\nabla \cdot \mathbf{u} = 0$, namely

$$\frac{\partial \psi}{\partial t} + \nabla \cdot (\mathbf{u}\psi) = 0. \tag{2}$$

With the level set transport equation written in conservative form, and the given definition of ψ, it is clear that the scalar ψ should be a conserved quantity. As in the case of the distance level set function ϕ, nothing insures that solving Eq. (2) will preserve the form of the hyperbolic tangent profile ψ. As a result, an additional

re-initialization equation needs to be introduced to re-establish the shape of the profile. This equation is written as

$$\frac{\partial \psi}{\partial \tau} + \nabla \cdot (\psi(1 - \psi)\mathbf{n}) = \nabla \cdot (\varepsilon(\nabla\psi \cdot \mathbf{n})\mathbf{n}), \tag{3}$$

and is advanced in pseudo-time τ. It consists of a compression term on the left-hand side that aims at sharpening the profile, and of a diffusion term on the right-hand side that ensure the profile remains of characteristic thickness ε, and therefore is resolvable on a given mesh. While ε is assumed constant here, thus requiring a uniformly spaced mesh around the interface, this assumption is formally unnecessary. ε can be made a function of space, allowing for a variable hyperbolic tangent thickness, and therefore making this method useable on non-uniform meshes. It should be noted that this equation is also written in conservative form. As a result, solving successively for Eqs. (2) and (3) should accomplish the transport of the $\psi = 0.5$ iso-surface, preserve the shape of the hyperbolic tangent profile, and ensure the conservation of ψ.

The CLS method of Olsson et al. [7,12] aims at reducing the mass conservation errors associated by exploiting the discrete conservation of the scalar ψ. In the limit where the thickness ε of the hyperbolic tangent profile ψ goes to zero, the volume integral of the ψ function approaches the volume enclosed in the $\psi = 0.5$ iso-surface, namely

$$\lim_{\varepsilon \to 0} \int_V \psi(\mathbf{x}; t)\, \mathrm{d}\mathbf{x} = \int_V H(\psi(\mathbf{x}; t) - 0.5)\, \mathrm{d}\mathbf{x}, \tag{4}$$

where H is the Heaviside function and V is a volume. Since all the equations that need to be solved for ψ are conservative, discrete conservation of the volume enclosed in the interface becomes possible. Clearly, for a given numerical mesh with a spacing Δx, taking $\varepsilon \ll \Delta x$ would lead to strong under-resolution of the hyperbolic tangent profile, and hence the numerical transport and re-initialization of ψ would suffer from severe numerical problems. In order to sufficiently resolve ψ, Olsson and Kreiss [7] proposed to use $\varepsilon = \Delta x/2$, which leads to an hyperbolic tangent profile represented on two to three mesh points. With such a discretization of the profile, discretely solving Eqs. (2) and (3) becomes possible. However, the volumetric integral of ψ does not exactly correspond to the volume enclosed in the $\psi = 0.5$ iso-surface. Consequently, the volume enclosed in the $\psi = 0.5$ iso-surface will not be discretely conserved. Olsson and Kreiss [7] observed, however, that such an approach greatly reduced the conservation errors. The underlying conservation of ψ provides an anchor to the $\psi = 0.5$ iso-surface, preventing the accumulation of transport and re-initialization inaccuracies leading to large mass conservation errors. In their numerical tests, Olsson and Kreiss [7] obtained very encouraging results where discrete conservation errors were reduced by an order of magnitude in comparison to classical level set approaches.

2.1.2. Computation of the interface normals

In their first paper, Olsson and Kreiss [7] mentioned that their choice of numerical method for the transport of the quantity ψ was based on three considerations:

- The discrete conservation of the transport should be ensured.
- No spurious oscillations should be introduced.
- The thickness of the hyperbolic tangent profile should be kept constant.

The first point is straightforward, and verified by most numerical methods. Similarly, the third point should be verified by solving the re-initialization equation for the hyperbolic tangent profile, Eq. (3). However, the second point is both expensive and difficult to enforce in general. Indeed, the cost of total variation diminishing (TVD)

schemes is typically more than the cost of simple non-TVD transport schemes, and their effectiveness is also conditioned on the divergence-free quality of the velocity field. In complex, realistic, turbulent simulations, ensuring that the velocity field is discretely divergence free to machine accuracy is a challenge. As a result, we can say that avoiding spurious oscillations, although desirable, is impossible to achieve in general. Consequently, the robustness of the method should not be based on this property. However, Olsson et al. [7,12] compute their normal vectors using

$$\mathbf{n} = \frac{\nabla \psi}{|\nabla \psi|}. \tag{5}$$

While this method is convenient because it uses a level set field that is readily available, it is however strongly sensitive to spurious oscillations. Indeed, an oscillation in ψ will appear as a large change in direction of the normal vector. As a result, the normals obtained by Eq. (5) are not appropriate to use in the re-initialization equation, Eq. (3). This equation contains a compression term that moves the level set scalar ψ along the directions defined by the normal vectors in order to re-form a hyperbolic tangent function. It can be expected that having normals that simply point in the wrong direction will lead to severe numerical difficulties. More precisely, the compression term will create an accumulation of ψ where the normal vectors are facing each others. In the presence of parasitic oscillations of the normal vectors, this means that spots of the scalar ψ will form spuriously in the domain, leading to an unphysical displacement of the liquid mass. To illustrate this point, we perform a few steps of the Zalesak's disk test case [13] usually employed to assess the accuracy of level set methods. The transport equation for the level set function is solved using a non-TVD scheme without re-initialization. It can be observed in Fig. 1(a) that the resulting normal vectors alternate direction, as can be expected from taking the gradient of a field with spurious oscillations.

In order to remedy this problem, we propose to recompute ϕ from the ψ function first using a standard re-distancing algorithm, then to use

$$\mathbf{n} = \frac{\nabla \phi}{|\nabla \phi|} \tag{6}$$

to compute the normals from the smooth, reconstructed distance function ϕ. This distance reconstruction can be performed efficiently using the fast marching method (FMM) [14], therefore it does not affect the overall cost of the method significantly. The specific cost increase due to the FMM is discussed in comparison with the cost of a TVD scheme in Ref. [4]. Moreover, the distance ϕ

for the points closest to the interface can simply be obtained by inverting the hyperbolic tangent function, meaning that no spurious displacement of the interface will be induced by this operation. It is then straightforward to access the interface normals by Eq. (6). We can see in Fig. 1(b) that the resulting normals are smooth, and will be perfectly useable to perform the re-initialization.

Having modified the way the normal vectors are computed, it is not necessary anymore to use non-oscillatory schemes for the level set transport. Therefore, we can take advantage of fast, high order, non-TVD scalar transport scheme. A commonly used approach is the high order upstream central (HOUC-n, where n is the order of the scheme) class of schemes, employed, for example, by Nourgaliev and Theofanous [15] for level set transport. The resulting method combines the good mass conservation properties of the standard CLS with greatly improved accuracy, at the additional cost of an FMM step. The FMM is found to be inexpensive in comparison to the cost of the level set transport, hence the overall cost of the ACLS scheme is comparable to that of a standard level set approach. This method is implemented in the context of a numerical code developed for accurate simulations of turbulent reactive flows, NGA [16].

2.1.3. ACLS solution procedure

Several more details about the method, including the conservative re-initialization and the accurate computation of the surface curvature are described in Desjardins et al. [4]. A brief summary of the ACLS solution procedure is given here:

- Using a semi-implicit Crank–Nicolson time integration, advance the ψ field by solving Eq. (2). HOUC-5 will be used for this step.
- Use FMM to efficiently reconstruct ϕ from ψ.
- Compute the face normals from ϕ.
- Compute the least-squares curvature from ϕ.
- Perform the conservative re-initialization step: Using a semi-implicit Crank–Nicolson time integration, Eq. (3) is advanced.

2.2. Flow solver coupling

The ACLS method is coupled with the flow solver NGA [16], which solves the variable density, low Mach number Navier–Stokes equations using high order conservative finite difference methods that are staggered in time and space. Such methods have been shown to be highly suited for turbulence simulation [16],
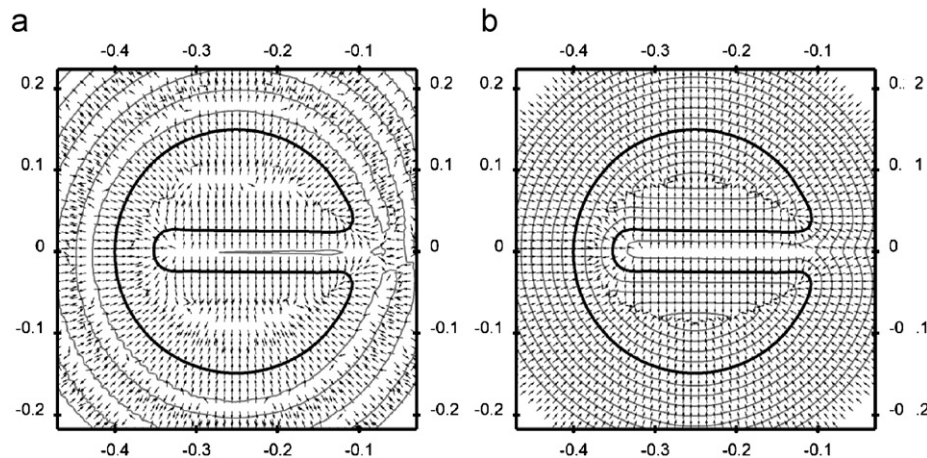

Fig. 1. Computation of interface normals in the presence of spurious oscillations in ψ. (a) Normals from ψ. Interface location (black line), and iso-contours of ψ (gray lines). (b) Normals from ϕ. Interface location (black line), and iso-contours of ϕ (gray lines).

and therefore are expected to be highly beneficial for ensuring the accuracy of turbulent multiphase simulations. The Navier–Stokes equations are solved using the classical fractional step approach [17]. In order to handle the large density variation across the phase interface, this code was modified to solve the incompressible Navier–Stokes equations by assuming constant density. The GFM [10,11] is then used to account explicitly for the density jump and the surface tension through the pressure term. The formulation of GFM in the present context is described in Desjardins et al. [4]. To verify the method, surface tension-driven instabilities have been computed and compared with an analytic dispersion relation. The results are reported in Desjardins et al. [4].

2.3. DNS of primary atomization

Several turbulent flow applications are of interest and will be studied in the context of DNS. Generation of a database of DNS results for the following test cases is planned: (1) turbulent atomization of liquid jets, (2) air-assisted atomization of co-annular liquid jets, and (3) liquid jets in crossflow. These

Table 1
Physics parameters for the liquid jet atomization test case

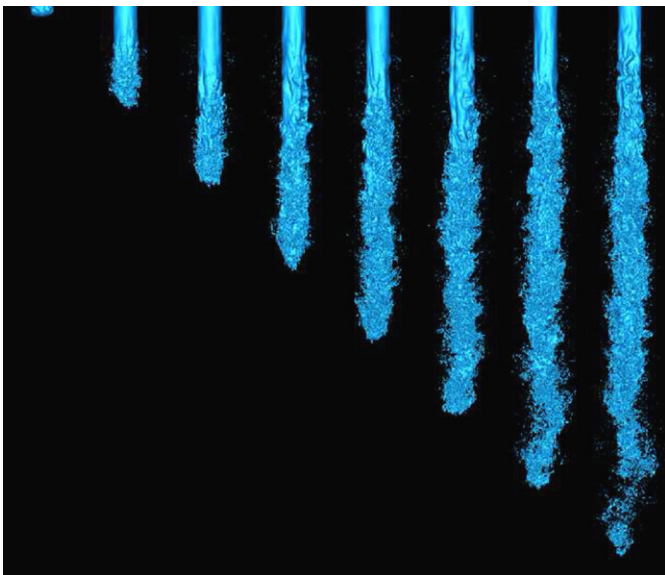| ρ_l/ρ_g	μ_l/μ_g	Re_l	We_l
40	40	3000	10000

Fig. 2. Turbulent atomization of a liquid diesel jet. The time interval between two frames is $\Delta t = 2.5$ based on the nozzle diameter and jet bulk velocity.

simulations will provide data to develop and test LES models, and will contribute to improve our understanding of the physical phenomena involved in turbulent liquid atomization.

In order to assess the performance of the proposed approach in the presence of fully developed turbulence, we conduct the simulation of a turbulent liquid jet in quiescent air. The properties for the simulation are inspired by liquid diesel injection systems, although both the Reynolds number and Weber number have been reduced to make the simulation possible. The parameters employed are summarized in Table 1.

No sub-grid scale model is employed for this simulation, even though it seems likely that the smallest structures are not fully resolved. This simulation can provide some much needed insights, both on the resolution requirements to simulate turbulent atomization, and on the performance of the present method in the context of turbulent flows. The computation is performed on a domain of size $24D \times 3D \times 3D$, where D is the jet diameter, discretized on a $1024 \times 128 \times 128$ mesh. The inflow conditions are obtained by first simulating a turbulent pipe using the liquid properties, and storing the time-dependent velocity information. This information is then re-injected into the computational domain.

Instantaneous snapshots of the interface at different times are presented in Fig. 2. The time interval between two frames is $\Delta t = 2.5$ based on the nozzle diameter and jet bulk velocity. The interface displays a complex turbulent behavior, as the liquid jet undergoes turbulent atomization. Many complex phenomena interact, leading to a fast break-up of the liquid core into ligaments and sheets, then droplets. It is interesting to note that by the end of the computational domain, the liquid core has fully disintegrated. The magnitude of the velocity and vorticity fields are presented in two-dimensional cuts in Fig. 3. The fully developed nature of the turbulence appears clearly. Even for such a complex, turbulent, three-dimensional flow, the proposed multiphase method appears robust.

Finally, we compare the mass enclosed in the $\psi = 0.5$ iso-contour with the exact expected liquid mass as a function of time in Fig. 4. With a maximum of 3% mass loss, the method proves very satisfactory in terms of mass conservation, even in a complex turbulent case.

These results are very encouraging, and suggest that full DNS of such a problem is feasible with this approach. Mesh refinement studies and parameter variations will complete this preliminary work.

3. Accurate dynamic model for sub-filter scalar variance

The second topic addressed here is the modeling of the sub-filter scalar variance. In LES, sub-filter modeling is always necessary, but the simulation results are often not too sensitive to the chosen model. The reason is that most of the turbulence
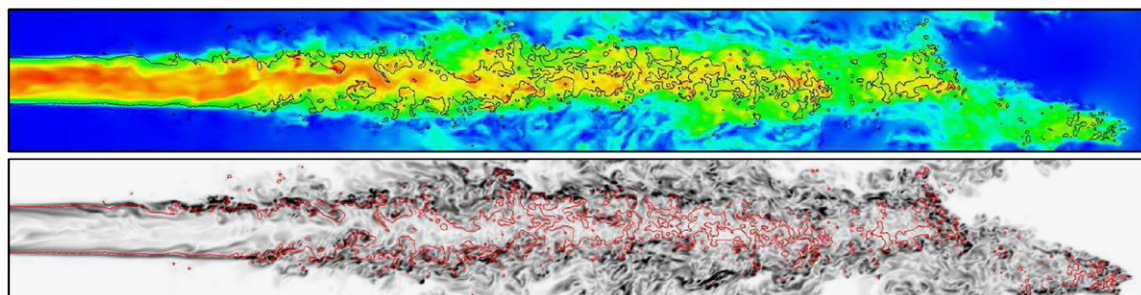

Fig. 3. Magnitude of the velocity (top) and vorticity (bottom) for the turbulent liquid jet case.
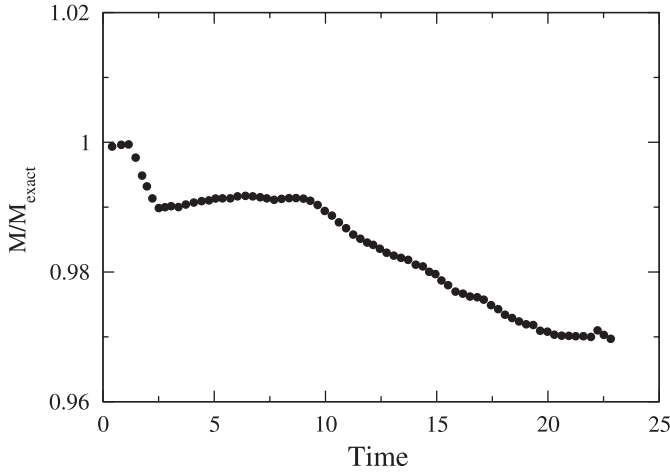
Fig. 4. Mass conservation errors for the turbulent liquid jet case.

energy is at the resolved large scales, which are usually dynamically important. However, it was mentioned above that for combustion problems, this may not be the case, because the heat release, which occurs at the smallest scales, substantially changes the flow field on the large scales. For combustion in technical devices, often the so-called mixed-is-burned, or in other words, the infinitely fast chemistry model is used. Although this is typically not correct, the heat release is usually mostly controlled by mixing. Therefore, quantities describing sub-filter mixing, i.e. the sub-filter scalar variance and dissipation rate, have to be determined accurately in combustion LES.

In a later section, we will present simulations of NO_x formation in aircraft engines. The combustion model used is the flamelet/progress variable (FPV) model [18]. In this framework, the quantities needed to be modeled are the sub-filter variance and the sub-filter dissipation rate of the mixture fraction. The mixture fraction is a conserved scalar used to describe mixing between fuel and oxidizer. The sub-filter variance is first required to define the sub-filter mixture-fraction distribution [19], and is defined as $Z_v = \overline{ZZ} - \bar{Z}\bar{Z}$, where $\bar{Z}$ is the filtered field of the mixture fraction Z. The filtered scalar dissipation rate is defined as

$$\bar{\chi} = 2D\overline{\frac{\partial Z}{\partial x_i}\frac{\partial Z}{\partial x_i}}$$

where D is the molecular diffusivity [1].

Here we will summarize the work of Balarac et al. [5,20], where sub-filter models for sub-filter mixing have been assessed using the concept of optimal estimators and a new dynamic sub-filter model has been proposed. To assess the accuracy of existing models, a priori tests are first conducted using DNS data from a forced homogeneous isotropic turbulence performed on 256^3 gridpoints. The numerical code used is a standard pseudo-spectral code. The Reynolds number based on the Taylor micro-scale and the rms of the velocity fluctuations is around 100. The molecular Schmidt numbers is 0.7. In the a priori tests, a box filter is chosen.

3.1. Previous sub-filter scalar variance models

Several models for the sub-filter variance have been proposed in the past [19,21]. The scale-similarity model [19] uses the self-similar behavior of turbulent properties at different length scales to model the sub-filter variance. The scalar variance is then written as

$$Z_{v,SS} = C_s(\overline{\bar{Z}\bar{Z}} - \hat{\bar{Z}}\hat{\bar{Z}}). \tag{7}$$

In this equation, $\hat{}$ denotes a test filter and C_s is the scale-similarity constant that needs to be specified. C_s is highly flow dependent and is not a universal constant. Hence, a priori specification almost always introduces large errors [22]. Pierce and Moin [21] proposed a dynamic formulation that is based on mixing length hypothesis similar to the Smagorinsky model. In this approach, the model constant is evaluated as a varying parameter using the filtered-fields available in LES. A scalar-gradient-based scaling law is used to obtain a closed-form algebraic equation for the sub-filter variance

$$Z_{v,DM} = C_d\Delta^2\frac{\partial \bar{Z}}{\partial x_i}\frac{\partial \bar{Z}}{\partial x_i}, \tag{8}$$

where Δ is the filter width and C_d is the model constant that is determined dynamically. Assuming that the model coefficient varies slowly in space and that the same coefficient applies at both filter levels, Eq. (8) can be filtered at the test-filter level leading to

$$\widehat{\overline{ZZ}} - \widehat{\bar{Z}\bar{Z}} = C_d\Delta^2\widehat{\frac{\partial \bar{Z}}{\partial x_i}\frac{\partial \bar{Z}}{\partial x_i}} \tag{9}$$

or it can be written at the test filter level, which gives

$$\widehat{\overline{ZZ}} - \hat{\bar{Z}}\hat{\bar{Z}} = C_d\hat{\Delta}^2\frac{\partial \hat{\bar{Z}}}{\partial x_i}\frac{\partial \hat{\bar{Z}}}{\partial x_i}, \tag{10}$$

where $\hat{\Delta}$ is the test filter width. Subtracting Eq. (9) from Eq. (10) then yields

$$L_d = C_d M_d \quad \text{with } L_d = \widehat{\bar{Z}\bar{Z}} - \hat{\bar{Z}}\hat{\bar{Z}} \text{ and}$$

$$M_d = \hat{\Delta}^2\frac{\partial \hat{\bar{Z}}}{\partial x_i}\frac{\partial \hat{\bar{Z}}}{\partial x_i} - \Delta^2\widehat{\frac{\partial \bar{Z}}{\partial x_i}\frac{\partial \bar{Z}}{\partial x_i}}. \tag{11}$$

Assuming that the coefficient is constant over homogeneous directions, C_d is then obtained using a least-squares averaging procedure

$$C_d = \frac{\langle L_d M_d \rangle}{\langle M_d M_d \rangle}, \tag{12}$$

where the brackets indicate averaging over homogeneous directions. Note that in the case of homogeneous turbulence, C_d is constant in the domain.

3.2. Error analysis using optimal estimators

As a first step towards understanding modeling errors, both these models were evaluated a priori using DNS data. For these tests, the scale similarity constant was taken to be equal to unity [19]. The models are compared using the notion of an optimal estimator [23]. Based on this idea, if a quantity Z_v is modeled with a finite set of variables ϕ, an exact model cannot be guaranteed. If the exact solution Z_v is known, for example from DNS, the optimal estimator of Z_v in terms of the set of variables ϕ is given by the expectation of the quantity Z_v conditioned on the variables in the set, i.e. $\langle Z_v|\phi \rangle$. The error with respect to the optimal estimator ε_{min} can consequently be defined as the averaging of the square of the difference at each point between the conditional mean value given by the value of ϕ at this point and the exact value of the quantity,

$$\varepsilon_{min} = \langle (Z_v - \langle Z_v|\phi \rangle)^2 \rangle, \tag{13}$$

where the angular brackets indicate statistical averaging over a suitable ensemble. It should be noted that any model formulated using the variable set ϕ will introduce an error that is larger than or equal to this minimum error ε_{min}, with the best model formulation producing this minimum error. Consequently, this

quadratic error is referred to as the irreducible error. Only a change in the variable set may reduce the magnitude of this error.

For the dynamic Smagorinsky-type model, the variable set used is

$$\phi_{DM} = \left\{ \frac{\partial \bar{Z}}{\partial x_i} \frac{\partial \bar{Z}}{\partial x_i} \right\},$$

whereas the variable set for the scale-similarity model is

$$\phi_{SS} = \{ \widehat{\bar{Z}\bar{Z}} - \hat{\bar{Z}}\hat{\bar{Z}} \}.$$

Note that the variables used to define C_d in the dynamic formulation are not taken into account, since C_d is constant due to the averaging process. Fig. 5 shows the quadratic errors of the scale-similarity and dynamic Smagorinsky-type models as function of the filter width. The irreducible errors associated with the corresponding variable sets are also shown. Both models are close to the irreducible error if the filter is in the dissipation range ($\Delta/\Delta x < 8$). When the filter is located in the inertial-convective range of the scalar spectrum, the quadratic errors of each model begin to be significantly larger than their associated irreducible errors. This is particularly true for the dynamic Smagorinsky-type model showing a very large error compared with the irreducible error for large filter size. If only the irreducible errors are compared, it is noticed that the irreducible error corresponding to the dynamic Smagorinsky-type model is always lower than the irreducible error corresponding to the scale-similarity model. These results show that a better model can potentially be formulated with the variable set ϕ_{DM} than for variable set ϕ_{SS}, but that a substantial improvement is needed to achieve this goal.

While the dynamic Smagorinsky-type model produces a large quadratic error, the variable set corresponding to this model produces a relatively small irreducible error. This means that the assumptions that lead to the functional form of the model formulation introduce the errors observed in the *a priori* tests. To understand the source of these errors, the main assumptions that lead to the dynamic formulation were studied in Balarac et al. [20]. It was shown that the assumption that leads to most of the

errors is that the coefficients in Eqs. (9) and (10) are the same, which implies that there is a strong scale dependence of the coefficient, which needs to be addressed. In this context, a new model formulation is discussed next.

3.3. Sub-filter scalar variance modeling based on Taylor series

The starting point for a new sub-filter scalar variance model is based on a Taylor series expansion. Considering a Gaussian filter, an expansion of $\overline{fg}$ as a function of $\bar{f}$ and $\bar{g}$ and their derivatives (where f and g are quantities describing flow fields) can be written as [24]

$$\overline{fg} = \bar{f}\bar{g} + \frac{\Delta^2}{12} \frac{\partial \bar{f}}{\partial x_i} \frac{\partial \bar{g}}{\partial x_i} + \frac{\Delta^4}{288} \frac{\partial^2 \bar{f}}{\partial x_i \partial x_j} \frac{\partial^2 \bar{g}}{\partial x_i \partial x_j} + \cdots . \quad (14)$$

If $f = u_i$ and $g = u_j$, and if only the first two terms of the right-hand side are considered, the gradient model proposed by Clark et al. [25] to model the sub-filter stress tensor is obtained. The Clark's relation can be used to model different types of sub-filter terms as long as the modeled terms have the most part of their energy at large scales, because otherwise, the truncation error of the expansion will be too large. For instance, da Silva and Pereira [26] have recently modeled successfully the sub-filter pressure–velocity term in the transport equation of the sub-filter kinetic energy using this relation.

Before deriving a new dynamic procedure, the dynamic Smagorinsky-type model assumptions can be examined in the light of expansion (14). We will start by deriving Eq. (10) from Eq. (14), which is the Smagorinsky-type model at the test filter scale. Note that in the derivation of the dynamic model, it is assumed that test-filtered quantities, such as $\hat{\bar{Z}}$ are obtained by first applying the filter on the regular scale and then applying the filter on the test-filter scale. Because of this, the modeling assumption used for Eq. (10) is not the same as that in Eq. (8). In fact, Eq. (8) follows from the mixing length assumption, whereas the model used in Eq. (10) would actually be the mixing length expression for $\widehat{\bar{Z}\bar{Z}} - \hat{\bar{Z}}\hat{\bar{Z}}$. Using expression (14) to expand $\widehat{\bar{Z}\bar{Z}}$ leads to

$$\widehat{\bar{Z}\bar{Z}} = \widehat{\bar{Z}}\widehat{\bar{Z}} + \frac{\Delta^2}{12} \frac{\partial \widehat{\bar{Z}}}{\partial x_i} \frac{\partial \widehat{\bar{Z}}}{\partial x_i} + \cdots$$
$$= \hat{\bar{Z}}\hat{\bar{Z}} + \frac{\hat{\Delta}^2}{12} \frac{\partial \hat{\bar{Z}}}{\partial x_i} \frac{\partial \hat{\bar{Z}}}{\partial x_i} + \frac{\Delta^2}{12} \widehat{\frac{\partial \bar{Z}}{\partial x_i} \frac{\partial \bar{Z}}{\partial x_i}} + \cdots . \quad (15)$$

Eq. (15) shows that $\widehat{\bar{Z}\bar{Z}} - \hat{\bar{Z}}\hat{\bar{Z}}$ cannot be described by the term $\hat{\Delta}^2 (\partial\hat{\bar{Z}}/\partial x_i)\partial\hat{\bar{Z}}/\partial x_i$ without taking the term $\Delta^2(\widehat{\partial\bar{Z}/\partial x_i})\partial\bar{Z}/\partial x_i$ into account. This shows that assumption (10) is incorrect. From this follows that Eq. (11), which is deduced from Eq. (10), cannot be used for the formulation of the dynamic procedure.

For the sub-filter scalar variance, the first order of expansion (14) leads to the model

$$Z_{v,o2} = \frac{\Delta^2}{12} \frac{\partial \bar{Z}}{\partial x_i} \frac{\partial \bar{Z}}{\partial x_i}, \quad (16)$$

which is similar to the dynamic Smagorinsky-type model, but using $C_d = \frac{1}{12}$ instead of computing C_d dynamically. One could use this constant value to compute the variance. However, since the higher order terms of the expansion are discarded in this model, a dynamic coefficient, C_n, can be introduced to account for the truncation error. The new formulation can be written as

$$Z_{v,NM} = C_n \Delta^2 \frac{\partial \bar{Z}}{\partial x_i} \frac{\partial \bar{Z}}{\partial x_i}. \quad (17)$$

Since the Leonard-term, $\widehat{\bar{Z}\bar{Z}} - \hat{\bar{Z}}\hat{\bar{Z}}$, is available in LES, the Taylor series expansion of this term can be used to determine the
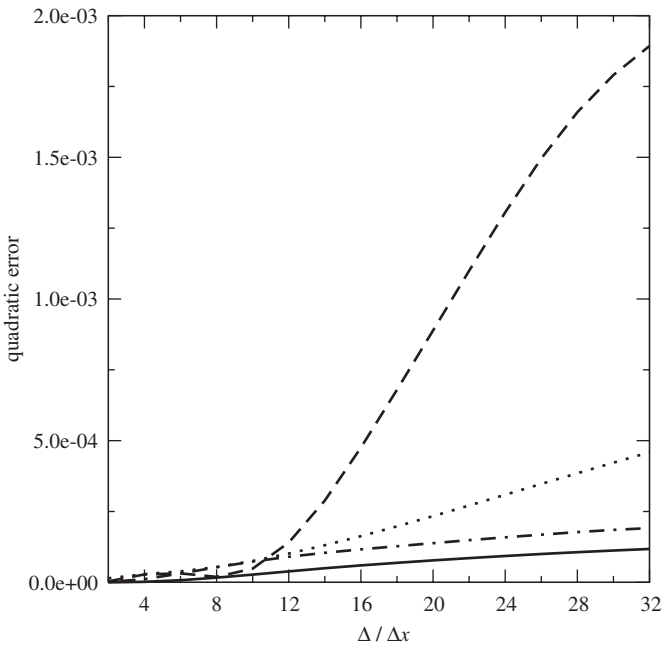

Fig. 5. Evolution of the quadratic errors of the scale similarity and dynamic Smagorinsky-type models and their associated irreducible error with the filter width. $\langle (Z_v - \langle Z_v | \phi_{DM} \rangle)^2 \rangle$ ——; $\langle (Z_v - Z_{v,DM})^2 \rangle$ - - - -; $\langle (Z_v - \langle Z_v | \phi_{SS} \rangle)^2 \rangle$ — · —; $\langle (Z_v - Z_{v,SS})^2 \rangle$ ·········.

dynamic coefficient. Expansion (14) is written for the test filter with $f = \bar{Z}$ and $g = \bar{Z}$. This leads to

$$\widehat{\bar{Z}\bar{Z}} - \hat{\bar{Z}}\hat{\bar{Z}} = \frac{\hat{\Delta}^2}{12}\frac{\partial \hat{\bar{Z}}}{\partial x_i}\frac{\partial \hat{\bar{Z}}}{\partial x_i} + \frac{\hat{\Delta}^4}{288}\frac{\partial^2 \hat{\bar{Z}}}{\partial x_i \partial x_j}\frac{\partial^2 \hat{\bar{Z}}}{\partial x_i \partial x_j} + \cdots. \tag{18}$$

Eq. (18) shows that $\widehat{\bar{Z}\bar{Z}} - \hat{\bar{Z}}\hat{\bar{Z}}$ can be evaluated from the derivatives of $\hat{\bar{Z}}$, which are also available in LES. Here, we keep only the first order term of the right-hand side, and introduce a dynamic coefficient to account for the truncation error. This coefficient is assumed to be equal to C_n, already used in Eq. (17).

To assess this assumption, the spatially dependent quantities C_1 and C_5 are defined as

$$\overline{ZZ} - \bar{Z}\bar{Z} = C_1 \Delta^2 \frac{\partial \bar{Z}}{\partial x_i}\frac{\partial \bar{Z}}{\partial x_i}, \tag{19}$$

and

$$\widehat{\bar{Z}\bar{Z}} - \hat{\bar{Z}}\hat{\bar{Z}} = C_5 \hat{\Delta}^2 \frac{\partial \hat{\bar{Z}}}{\partial x_i}\frac{\partial \hat{\bar{Z}}}{\partial x_i}. \tag{20}$$

From an instantaneous scalar field, local values of C_1 and C_5 for several filter sizes can be determined from Eqs. (19) and (20), respectively. From this, the PDFs of C_1 and C_5 can then be computed for given filter sizes. The PDFs of C_1 and C_5 from an instantaneous velocity field at a time after the simulation has reached steady state for several filter sizes are shown in Figs. 6 and 7, respectively. The distributions of both C_1 and C_5 are unimodal with distinct peaks. Moreover, the range of values of C_5 is close to the range of values of C_1. This confirms that the assumptions that C_1 and C_5 are constant over homogeneous directions and that $C_1 = C_5 = C_n$ are valid. To eliminate potential spurious oscillations due to the local values of the dynamic coefficient, C_n is assumed to be constant over statistically homogeneous directions. A simple average then yields

$$C_n = \frac{\langle L_n \rangle}{\langle M_n \rangle}, \tag{21}$$

with $L_n = \widehat{\bar{Z}\bar{Z}} - \hat{\bar{Z}}\hat{\bar{Z}}$ and $M_n = \hat{\Delta}^2(\partial\hat{\bar{Z}}/\partial x_i)\partial\hat{\bar{Z}}/\partial x_i$. Instead, C_n can also be evaluated from a least-squares approximation according to
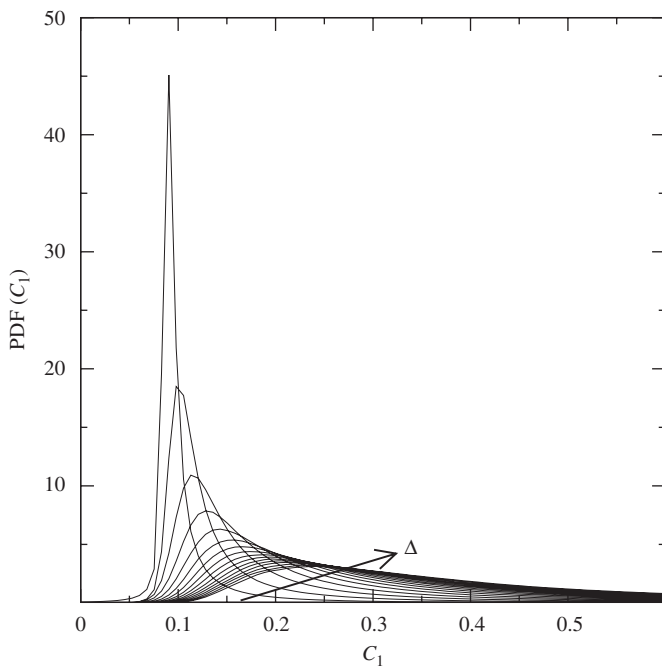

Fig. 6. PDF of C_1 (Eq. (19)) for several filter sizes. The arrow indicates increasing filter sizes.
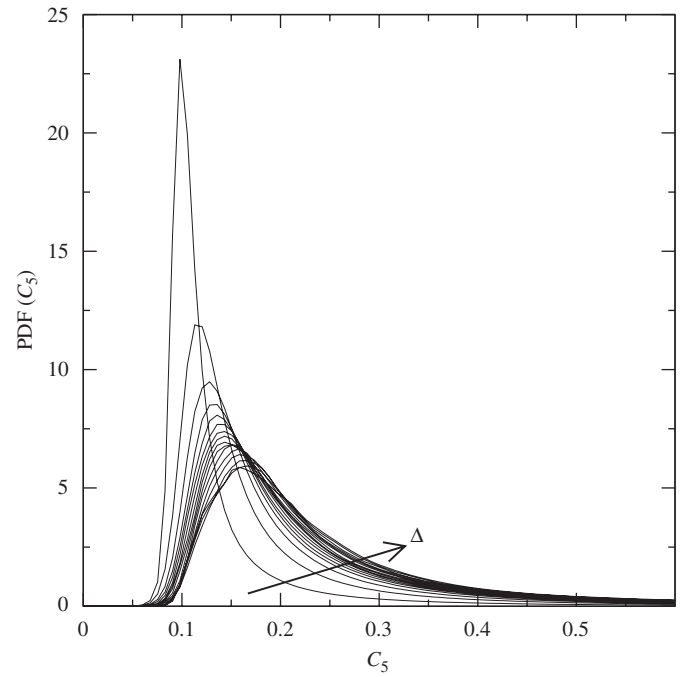

Fig. 7. PDF of C_5 (Eq. (20)) for several filter sizes. The arrow indicates increasing filter sizes.
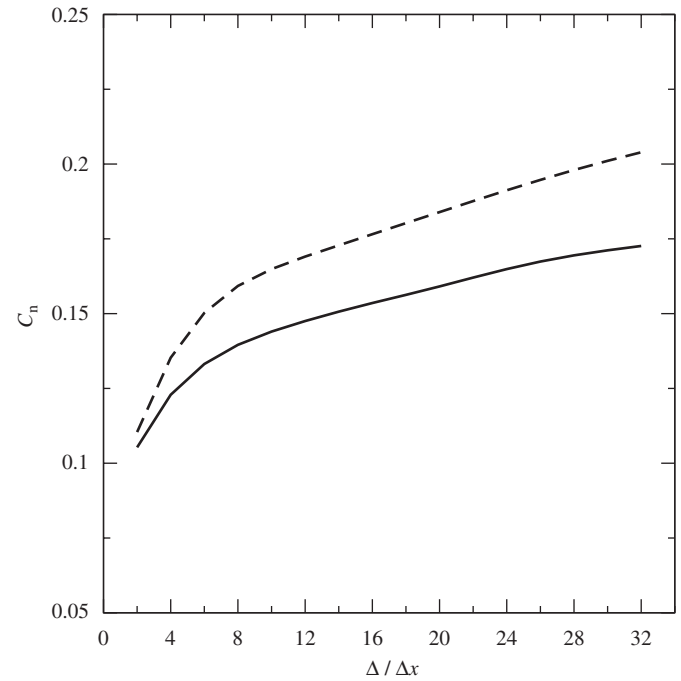

Fig. 8. Model constant computing following both ways given in Eqs. (21) and (22). $C_n = \langle L_n M_n \rangle / \langle M_n M_n \rangle$ ———; $C_n = \langle L_n \rangle / \langle M_n \rangle$ - - - -.

Lilly's method [27] as

$$C_n = \frac{\langle L_n M_n \rangle}{\langle M_n M_n \rangle}. \tag{22}$$

As shown in Fig. 8, both methods yield similar results. In the following, C_n is computed with the least-squares averaging. Note that the average needed for the dynamic procedure could be evaluated over statistically homogeneous directions, or, for flows in complex geometry, by using the Lagrangian dynamic procedure

proposed by Meneveau et al. [28], which evaluates averages over flow pathlines.

3.4. Performance of the new model

Expansion (14) is given assuming a Gaussian filter. Hence the question of validity of expansion (14) for the box filter is important, even though it is known that results are practically independent of the filter type when the box or the Gaussian filters are used [29,30]. Therefore, the box filter is used in the context of the *a priori* tests presented in the following.

Fig. 9 shows the quadratic errors for the different models. Note that the model $Z_{v,o2}$ given by Eq. (16) is also tested for comparison. For all filter sizes, the quadratic error of $Z_{v,NM}$ is smaller than the quadratic errors obtained with the two other models. Moreover, the quadratic error of the new dynamic procedure stays close to the irreducible error, whereas the quadratic error of the dynamic Smagorinsky-type model increases strongly. This shows that $Z_{v,NM}$ is close to the best possible model using only ϕ_{DM} as variable set. We can also note that the quadratic error of $Z_{v,NM}$ is very close to the irreducible error using ϕ_{SS} as set of quantities (Fig. 5). This shows that $Z_{v,NM}$ will be more accurate than a scale-similarity model independently of the scale-similarity constant C_s.

To assess the quality of a model, a scatter plot showing the model result, $g(\phi)$, versus the modeled quantity, Z_v, is often used. In the same spirit, Moreau et al. [23] proposed to consider $\langle Z_v | g(\phi) \rangle$ as a function of $g(\phi)$. They demonstrate that the model is optimal when $\langle Z_v | g(\phi) \rangle = g(\phi)$. Fig. 10 shows $\langle Z_v | Z_{v,model} \rangle = f(Z_{v,model})$ for several filter sizes. For the dynamic Smagorinsky-type model, the large quadratic errors for large filter sizes are due to an important under-prediction of the sub-filter scalar variance. The model $Z_{v,o2}$ always under-predicts the sub-filter scalar variance due to the truncation error, since all the terms of expansion (14) are positive. The proposed model appears to be very promising giving good results for all filter sizes. Finally, Fig. 11 shows the probability density functions of the sub-filter scalar variance predicted by each model for $\Delta/\Delta x = 14$. The models are compared with the sub-filter scalar variance, Z_v,
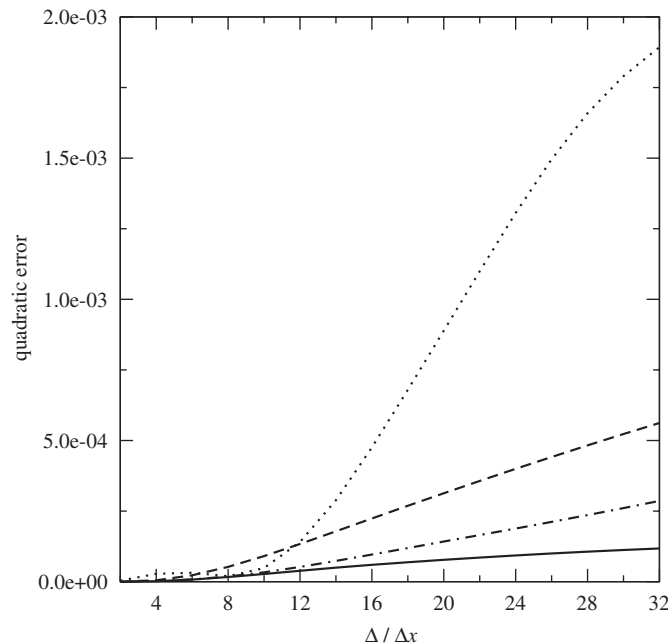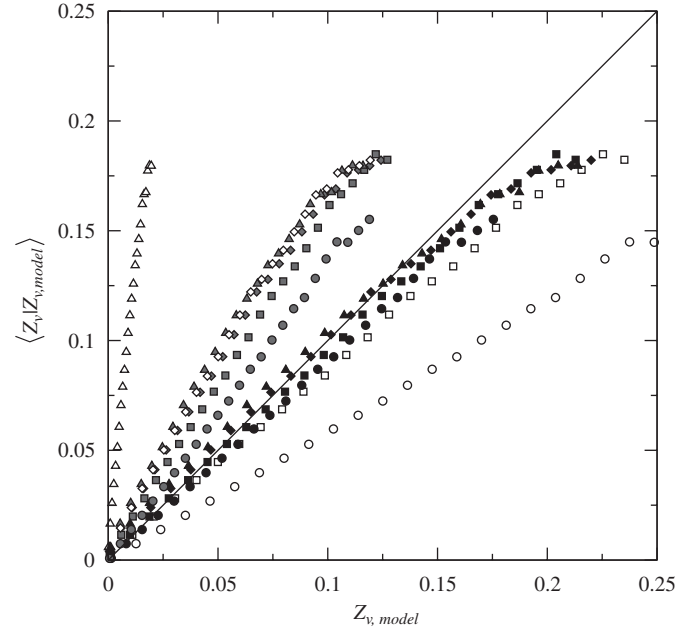
Fig. 10. Plot of $\langle Z_v | Z_{v,model} \rangle$ as a function of $Z_{v,model}$. $\Delta/\Delta x = 4$ ($\circ$), $\Delta/\Delta x = 8$ ($\square$), $\Delta/\Delta x = 12$ ($\diamond$), and $\Delta/\Delta x = 16$ ($\triangle$). $Z_{v,DM}$ (white), $Z_{v,o2}$ (gray) and $Z_{v,NM}$ (black). $y = x$ ——.
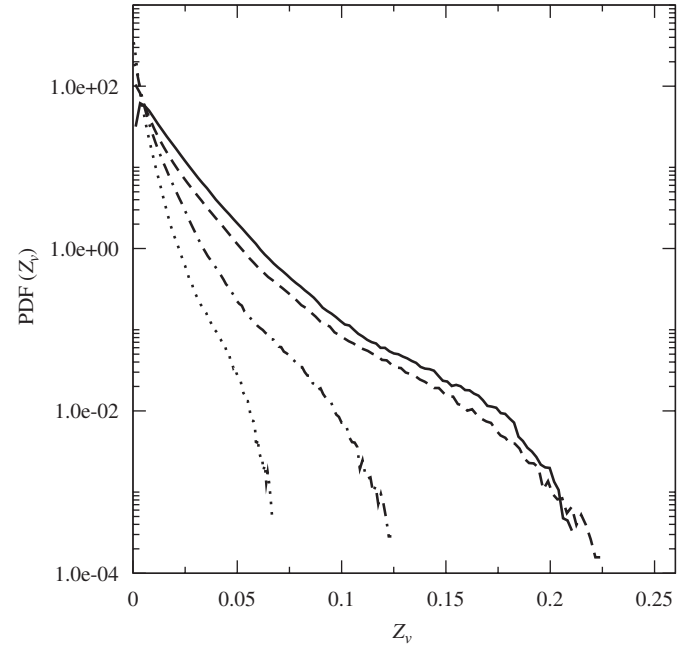
Fig. 11. PDF of the sub-filter scalar variance for $\Delta/\Delta x = 14$. Z_v ——; $Z_{v,DM}$ ·······; $Z_{v,o2}$ — · —; $Z_{v,NM}$ - - - -.

evaluated from the filtered DNS. As expected, the agreement between the new dynamic procedure, $Z_{v,NM}$, and the filtered DNS data is very good, whereas the other models under-predict the DNS data substantially.

4. Model for prediction of nitric oxide formation

Finally, we will address the topic of pollutant formation in aircraft engines. Both soot and oxides of nitrogen (NO_x) are

Fig. 9. Evolution of the quadratic errors of the models $Z_{v,DM}$, $Z_{v,o2}$ and $Z_{v,NM}$ and the associated irreducible error with the filter width. $\langle (Z_v - \langle Z_v | \phi_{DM} \rangle)^2 \rangle$ ——; $\langle (Z_v - Z_{v,DM})^2 \rangle$ ·······; $\langle (Z_v - Z_{v,o2})^2 \rangle$ - - - -; $\langle (Z_v - Z_{v,NM})^2 \rangle$ — · —.

important emissions from aircraft engines. As in most non-premixed combustion systems, there is a trade-off among the two. Typically faster mixing of fuel and air provides larger stoichiometrically premixed regions leading to more NO_x, while less mixing yields more soot. Therefore, lean premixed combustion processes are favored whenever possible. Lean premixed combustion, however, is prone to instabilities, which have to be avoided in aircraft engines. This is often accomplished by a staged combustion process, where a rich primary combustion region is followed by mixing with secondary air.

In this section, a model for the prediction of the nitrogen oxide formation by Ihme and Pitsch [6] is presented. The strong temperature sensitivity of NO formation requires the accurate description of the instantaneous temperature field in a flame under the consideration of radiative heat loss effects, which requires a radiation model, which needs to be integrated into the combustion model. Here the method developed by Ihme and Pitsch [6] is employed. This model is based on a flamelet table, which is parameterized in terms of mixture fraction Z, reaction progress variable C, and enthalpy H. The table contains certain species mass fractions, density, and certain source terms that are required by the NO_x model as described below. In the next section, a model for NO formation is presented. Following this, a closure model for application in LES is developed. The model is then applied in LES of Sandia flame D and a Pratt and Whitney aircraft engine combustor configuration.

4.1. Model formulation

Similar to the radiation process, NO formation, particularly via the thermal mechanism, occurs on a relatively long time scale compared to the life time of a flame element in the flow. This observation suggests that NO is not in steady state, and a steady-state assumption will consequently result in considerable over-predictions of NO.

The slow spatial and temporal formation and consumption of NO is described in the present model by the separate solution of a transport equation for the NO mass fraction, Y_{NO}. Under the assumption of equal species diffusivities, this equation can be written as

$$\rho \mathscr{D}_t Y_{NO} = \nabla(\rho \alpha \nabla Y_{NO}) + \rho \dot{\omega}_{NO}. \tag{23}$$

In the following, we will extract the chemical production rate of NO from the extended FPV model, i.e. $\dot{\omega}_{NO} = \mathscr{G}^e_{\dot{\omega}_{NO}}(Z, C, H)$, where $\mathscr{G}$ denoted the flamelet library, which is parameterized in terms of Z, C, and H. This, however, requires special attention, and is explained by considering the following elementary model reaction:

$$A + B \underset{k_b}{\overset{k_f}{\rightleftarrows}} NO + D,$$
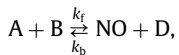
in which species A and B react to form products NO and D. Here, k_f and k_b denote the rate coefficients of the forward and backward reaction, respectively. For this reaction, the chemical reaction rate of NO can be written as

$$\dot{\omega}_{NO} = \dot{\omega}^+_{NO} + \dot{\omega}^-_{NO}, \tag{24}$$

with the production and consumption rate of the form

$$\dot{\omega}^+_{NO} = \frac{W_{NO}}{\rho^{FPV}} k_f^{FPV} \left(\frac{\rho^{FPV} Y_A^{FPV}}{W_A} \right) \left(\frac{\rho^{FPV} Y_B^{FPV}}{W_B} \right), \tag{25a}$$

$$\dot{\omega}^-_{NO} = -Y_{NO}^{FPV} k_b^{FPV} \left(\frac{\rho^{FPV} Y_D^{FPV}}{W_D} \right). \tag{25b}$$

Since reaction rates will be taken from the flamelet library, all species in (25) correspond to the conditions of the flamelet library, and are explicitly denoted by the superscript "FPV."

In the following, it is assumed that all species except NO are formed on relatively short time scales, and can therefore be represented by the FPV library. Since $\dot{\omega}^-_{NO}$ is a function of Y_{NO}^{FPV}, the consumption rate is adjusted using the computed NO mass fraction from Eq. (23). Thus, the modeled NO production rate can be written as

$$\dot{\omega}_{NO} = \dot{\omega}^+_{NO} + Y_{NO} \frac{\dot{\omega}^-_{NO}}{Y_{NO}^{FPV}}. \tag{26}$$

It is interesting to note that this model converges to that of the unsteady flamelet model, since in this case $Y_{NO} = Y_{NO}^{FPV}$, ensuring model consistency.

Although the model given by (25) was here written for a simple one-step NO formation reaction, it can be used for general detailed reaction schemes by expressing $\dot{\omega}^+_{NO}$ and $\dot{\omega}^-_{NO}$ in terms of the total NO production and consumption rates, respectively. The validity of this model was analyzed in comparison with the detailed results of an unsteady flamelet model. The unsteady flamelet model correctly captures the different time scales of mixing, mean flow, radiation, and formation of different chemical species, and it was shown in the past that this model predicts NO with good accuracy [2]. The comparison of the present NO model with the unsteady flamelet model was performed individually for the different NO formation mechanisms, thermal, prompt, and through N_2O. It was found that especially for the thermal NO mechanism, which is typically dominant in aircraft engines, the results of both models were in excellent agreement.

4.2. Application in LES

4.2.1. Turbulence closure

In an LES application, a transport equation for the Favre-filtered NO mass fraction $\widetilde{Y}_{NO}$ is solved. After multiplying Eq. (23) with the LES filter kernel G and spatial integration, this equation can be written as

$$\overline{\rho} \widetilde{\mathscr{D}}_t \widetilde{Y}_{NO} = \nabla \cdot (\overline{\rho} \widetilde{\alpha} \nabla \widetilde{Y}_{NO}) + \nabla \cdot \overline{\boldsymbol{\tau}}^{res}_{NO} + \overline{\rho} \widetilde{\omega}_{NO}, \tag{27}$$

and with the definition

$$\dot{\varpi}_{NO} \equiv \frac{\dot{\omega}^-_{NO}}{Y_{NO}^{FPV}} \tag{28}$$

the filtered production rate can be expressed as

$$\widetilde{\omega}_{NO} = \widetilde{\omega}^+_{NO} + \widetilde{Y}_{NO} \widetilde{\varpi}_{NO} + \widetilde{Y''_{NO} \varpi''_{NO}}, \tag{29}$$

where cross terms are neglected. The last term on the right-hand side accounts for residual scale correlations between the computed NO mass fraction and consumption rate. This term cannot directly be obtained from the flamelet library and requires modeling. In this work, closure is obtained by assuming scale similarity between Y_{NO} and Y_{NO}^{FPV}, which can be written as

$$\frac{\widetilde{Y}_{NO}}{\overline{Y}_{NO}^{FPV}} = \frac{Y''_{NO}}{Y_{NO}^{FPV''}}. \tag{30}$$

Here we assume that the steady-state NO fluctuations are proportional to the transient NO fluctuations. This assumption will only affect the last term in Eq. (29), which is typically small compared to the other two contributions. With this, Eq. (29) reduces to

$$\widetilde{\omega}_{NO} = \widetilde{\omega}^+_{NO} + \widetilde{Y}_{NO} \frac{\widetilde{\omega}^-_{NO}}{\widetilde{Y}_{NO}^{FPV}}. \tag{31}$$

The filtered source term contributions $\widetilde{\omega}^+_{NO}, \widetilde{\omega}^-_{NO}$, and $\widetilde{Y}_{NO}^{FPV}$ are precomputed using a presumed PDF and are stored in a flamelet library. Note that only these quantities are retrieved from the flamelet library, and that these quantities are well resolved in the

library. Hence, the model is not sensitive to the resolution of the chemistry table.

The proposed model for the prediction of NO-formation requires only the solution of two additional transport equations, namely equations for the filtered enthalpy and NO-mass fraction. The solution of these transport equations increases the computational complexity of the model only marginally, so that this extended FPV model remains computationally efficient.

4.2.2. Sandia flame D

The transport equation for the Favre-filtered NO mass fraction with the modeled source term, shown in Eq. (31), is solved in addition to the filtered scalar equations describing the evolution of mixture fraction, progress variable, and total enthalpy, constituting the extended radiative FPV model. This model is applied in LES of Sandia flame D, and results for the NO formation are presented in the following. More details of the configuration and about the combustion model and the numerical simulation can be found in Ihme and Pitsch [6]. Here, only some results are presented, and the effect of the interaction between turbulence, chemistry, and radiation on NO formation is quantified.

In Fig. 12, centerline profiles of the NO mass fraction from the simulations are compared with ensemble-averaged measurements. Additionally, results from the adiabatic simulation and the steady flamelet solution are shown. It can be seen that the predicted NO mass fraction from the adiabatic and radiative simulations are identical up to $x/D \approx 40$. This result can be expected, since both models predict an identical temperature evolution in this region [6]. The location of the peak formation is correctly predicted by the model; however, the peak NO mass fraction is over-predicted. It is interesting to point out that the adiabatic calculation considerably under-predicts the NO decrease in the fuel-lean part of the flame.

Mixture fraction-conditioned results at different axial locations in the jet flame are compared with experimental data in Ihme and Pitsch [6]. It is shown that the consideration of radiative heat losses results in an NO reduction in the conditional data by approximately 25–30%. The predictions from the radiative NO model are shown to be in good agreement with the unsteady flamelet model, at least up to $x/D = 30$. In conclusion, it is shown that the consideration of radiative effects is essential for the prediction of NO formation. It is demonstrated that the developed NO model yields considerably improved results compared with the steady flamelet model. NO predictions comparable with the unsteady flamelet model are obtained in the application of the model in the simulation of Sandia flame D. According to the results of the analysis presented in Ihme and Pitsch [6], NO predictions are expected to considerably improve for cases where thermal NO is dominant.

4.2.3. Pratt and Whitney combustor simulation

The successful validation against the Sandia flame experiment encouraged the application of the model to the Pratt and Whitney PW 6000 combustor configuration. The accurate prediction of NO emissions in aircraft engines at relevant operation conditions is important in the early design stage. The flow field inside the combustor is highly turbulent, swirling, and separated. The liquid fuel atomizes when entering the combustion chamber through the injector. In the combustion chamber the droplets of fuel interact further by collision or coalescence until they eventually evaporate. The spray flame is stabilized by a recirculation zone, which is created by a swirling flow. Furthermore, air is injected into the combustion chamber through multiple jets, resulting in complex mixing patterns.

Compared with RANS-based models, LES has the potential to predict these unsteady, three-dimensional, geometry-dependent, coherent flow features, and their sensitivity to changes in the combustor design [31,32]. Therefore, numerical simulations of the combustor configuration are performed using the unstructured, finite-volume LES solver CDP. The code includes models for the droplet motion, the breakup and evaporation of the spray, and the gas phase chemistry is described using the FPV model. The different models for the liquid phase are summarized in the following for completeness. Further details can be found in Moin and Apte [33] and reference therein.

The combustor simulations are performed for take-off condition. The pressure in the combustion chamber at this operating condition is 20 bar. A surrogate fuel, consisting of 82.6% n-decane ($C_{10}H_{22}$) and 17.4% trimethylbenzene (C_9H_{12}) by mass is used as fuel. The chemical mechanism considers 113 species among 491 chemical reactions [34]. Using this mechanism with the boundary conditions given in Table 2, flamelets are computed and compiled into a flamelet library. The simulations are performed for a 20° sector of the full combustor, which consists in total of 18 injectors. The computational grid consists of 3.64 million control volumes with finer resolution in the region of the injector and the dilution holes. The Reynolds number, which is based on the nozzle diameter, air inlet velocity, and kinematic viscosity of air at inlet conditions, is approximately 725,000.

Table 2
Conditions for the Pratt and Whitney combustor configuration

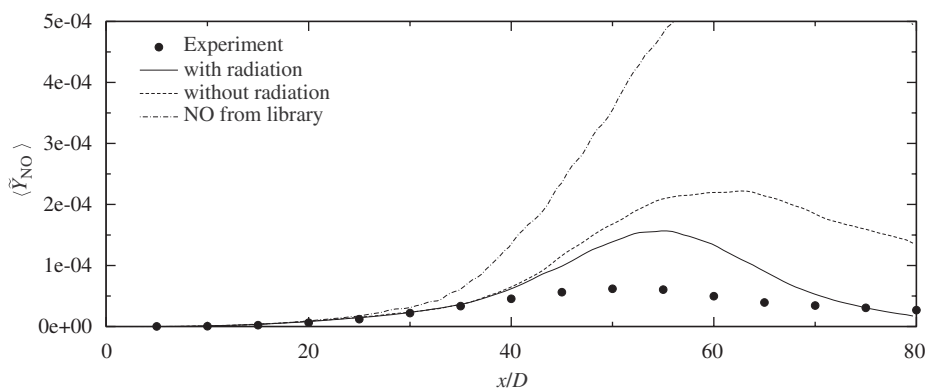| Parameter	Value
Stoichiometric condition (–)	$Z_{st} = 0.0635$
Fuel stream (–, K)	$Y_{C_{10}H_{22}} = 0.8256$, $Y_{C_9H_{12}} = 0.1744$, $\Theta = 171.4$
Oxidizer stream (–, K)	$Y_{O_2} = 0.233$, $Y_{N_2} = 0.767$, $\Theta = 812$
Pressure (bar)	20.0

Fig. 12. Comparison of measured (symbols) and calculated (lines) mean NO mass fraction along the centerline for Sandia flame D.
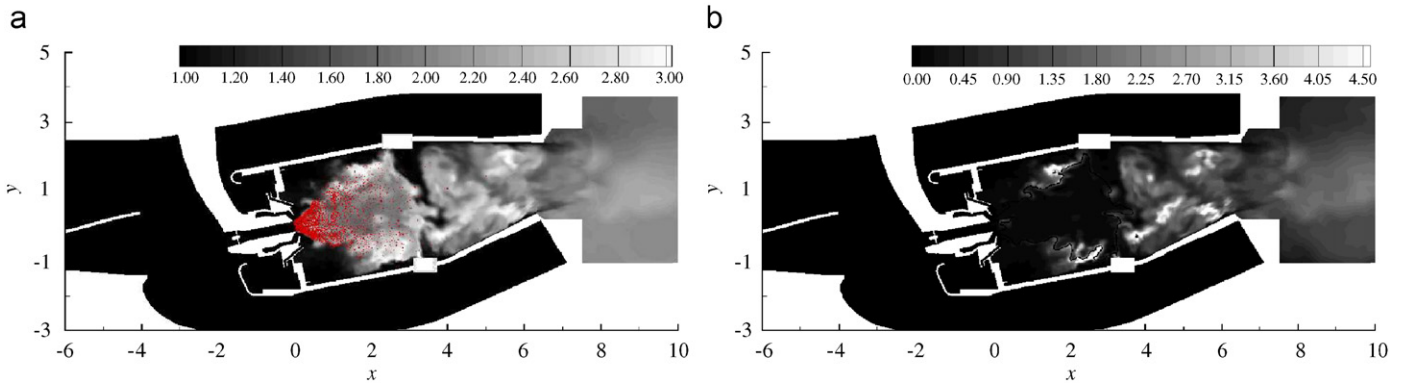
a

b

Fig. 13. Contours of the instantaneous and NO mole fraction along an axial cross section in a Pratt and Whitney aircraft engine combustor at take-off condition. The solid lines show the location of stoichiometric mixture ($Z_{st} = 0.0635$). (a) Instantaneous Favre-filtered temperature (normalized). (b) Instantaneous Favre-filtered NO mole fraction (normalized).

The Pratt and Whitney combustor is designed as rich-quench-lean (RQL) combustor system, incorporating separate zones of combustion to maintain stability while reducing emissions. Combustion is initiated in the fuel-rich zone, in which all fuel is injected. The fuel partially reacts in an oxygen-lean environment, and completes approximately 50% of the overall energy release. The combustion products in the fuel-rich zone consist mainly of CO and UHC and essentially no NO_x is formed [35]. The remaining air is rapidly injected in the quenching zone in order to reduce the combustion residence time near the stoichiometric condition. The reaction is completed past the quenching zone in the lean zone, providing the remaining energy release. In order to minimize NO_x emissions, it is essential to realize a rapid transition between the fuel-rich and fuel-lean zone to avoid long residence times around stoichiometric condition. In the following, the numerical results are discussed. Note that the dilution holes are not shown in the figures, and all results are normalized.

Fig. 13 shows instantaneous and averaged profiles of temperature and NO mole fraction along the axial plane through the combustor. The instantaneous droplet distribution is also shown in Fig. 13(a). The turbulent and complex flame structure and flow pattern can be observed in Figs. 13(a) and (b).

The instantaneous NO mole fraction is shown in Fig. 13(b). It can be seen that the NO formation in the primary zone is aligned with the surface of stoichiometric mixture (shown by the solid line), which is determined by the spray angle. Some NO formation on the fuel-rich side of the flame is evident, suggesting that the prompt mechanism is most relevant for its formation. During the transition through the quench zone, NO diffuses into the fresh air stream. Fig. 13(b) shows large regions with high concentration of NO on the fuel-lean side, which is an indication of Zeldovich NO. Also, the finite residence time of the gas mixture when passing through the quench zone might be partially responsible for NO formation.

The mean temperature and mean NO mole fraction at the combustor exit are compared next. Circumferentially averaged quantities are denoted by $\langle \cdot \rangle$. Mean quantities, which are denoted by $\langle \cdot_m \rangle$, are obtained from spatial averaging over the combustor exit plane.

The mean temperature obtained from the adiabatic simulation, non-dimensionalized with the experimentally reported mean temperature, is 1.0393. By accounting for the radiation effects, the exit temperature is 1.0437. The small increase of $\langle \widetilde{\Theta} \rangle_m$ is attributed to a shift in the location of the peak temperature. The comparison between experiments and simulation is summarized in Table 3. The computed exit temperature profiles and the exit profile factor are compared with experimental data in Fig. 14.

Table 3

Comparison between experiment and simulation for averaged mean temperature and NO mole fraction at combustor exit plane

	$\langle \widetilde{\Theta} \rangle_m / \langle \Theta \rangle_{Exp}$	$\langle \widetilde{X}_{NO} \rangle_m / \langle X_{NO} \rangle_{Exp}$
Experiment	1	1
Simulation with radiation	1.0437	1.3803
Simulation without radiation	1.0393	4.2254

Whereas the radiative simulation predicts a peak in the temperature profile at the centerline of the combustor, the temperature maximum obtained from the adiabatic simulation is shifted towards inner diameter.

The circumferentially averaged NO mole fraction is shown in Fig. 14(b). For reference, the dotted line indicates the normalized experimentally determined NO mole fraction. It can be seen that the location of the peak NO mole fraction shows good correlation with the peak temperature in Fig. 14. The predicted NO mole fraction computed with radiation and non-dimensionalized with the experimental measurements, is 1.3803, corresponding to an over-prediction of 38%. Note also that $\langle \widetilde{X}_{NO} \rangle$ from the adiabatic simulation is larger by a factor of approximately four than that from the radiative simulation.

5. Conclusions

In the present paper, we have addressed three different topics important for predictive large-eddy simulations of combustion in aircraft engines: the primary atomization process, the sub-filter scalar mixing process, and the formation of NO. To better understand the atomization process, a new numerical technique was developed, which is accurate, mass conserving, and relatively easy to implement. The method will be used in the future to perform direct numerical simulations of configurations relevant to aircraft engine fuel atomization, and in large-eddy simulations, once appropriate sub-filter models have been developed from the DNS results. To study the sub-filter scalar mixing process, existing model were analyzed using the concept of optimal estimators. A new dynamic model was proposed based on a series expansion of the sub-filter scalar fluctuation. The model was shown to be in excellent agreement with DNS data. Finally, a model describing NO formation in turbulent combustion was presented. The model integrates a radiation model, which was shown to be important for NO formation. The model is straightforward and therefore easy
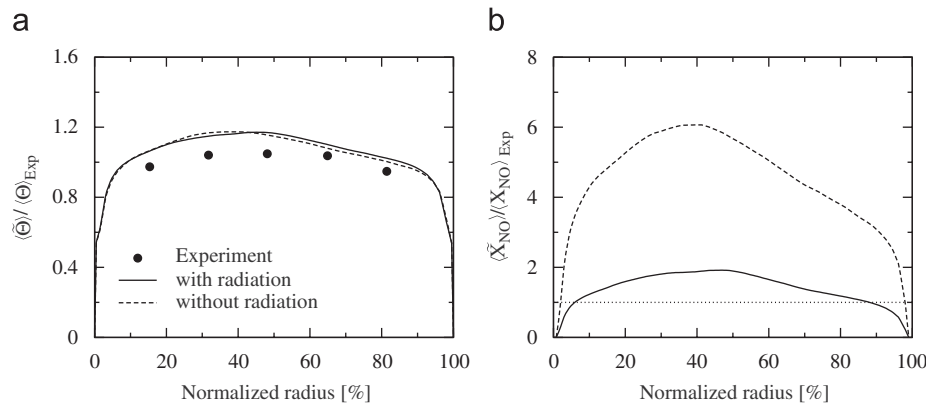
a

b

Fig. 14. Azimuthally averaged statistics at combustor exit plane: (a) normalized temperature and (b) NO mole fraction.

to implement, even in complex simulation codes. Simulations of NO formation in an aircraft engine at take-off is shown to be in very good agreement with experimental data.

References

[1] Pitsch H. Large-eddy simulation of turbulent combustion. Ann Rev Fluid Mech 2006;38:453–83.

[2] Pitsch H. Improved pollutant predictions in large-eddy simulations of turbulent non-premixed combustion by considering scalar dissipation rate fluctuations. Proc Combust Inst 2002;29:1971–8.

[3] Raman V, Pitsch H. Large-eddy simulation of a bluff-body stabilized flame using a recursive-refinement procedure. Comb Flame 2005;142:329–47.

[4] Desjardins O, Moureau V, Pitsch H. An accurate conservative level set/ghost fluid method for simulating turbulent atomization, J Comput Phys 2008; 227(18):8209–488.

[5] Balarac G, Pitsch H, Raman V. Development of a dynamic model for the subfilter scalar variance using the concept of optimal estimators. Phys Fluids 2008;20:035114.

[6] Ihme M, Pitsch H. Modeling of radiation and NO formation in turbulent non-premixed flames using a flamelet/progress variable formulation, Phys Fluids 2007; in press.

[7] Olsson E, Kreiss G. A conservative level set method for two phase flow. J Comput Phys 2005;210:225–46.

[8] Enright D, Fedkiw R, Ferziger J, Mitchell I. A hybrid particle level set method for improved interface capturing. J Comput Phys 2002;183:83–116.

[9] Sussman M, Puckett EG. A coupled level set and volume of fluid method for computing 3D and axisymmetric incompressible two-phase flows. J Comput Phys 2000;162:301–37.

[10] Fedkiw R, Aslam T, Merriman B, Osher S. A non-oscillatory Eulerian approach to interfaces in multimaterial flows (the ghost fluid method). J Comput Phys 1999;152:457–92.

[11] Kang M, Fedkiw R, Liu X-D. A boundary condition capturing method for multiphase incompressible flow. J Sci Comput 2000;15:323–60.

[12] Olsson E, Kreiss G, Zahedi S. A conservative level set method for two phase flow II. J Comput Phys 2007;225:785–807.

[13] Zalesak ST. Fully multidimensional flux-corrected transport algorithms for fluids. J Comput Phys 1979;31:335–62.

[14] Sethian JA. Level set methods and fast marching methods. 2nd ed. Cambridge, UK: Cambridge University Press; 1999.

[15] Nourgaliev RR, Theofanous TG. High-fidelity interface tracking in compressible flows: unlimited anchored adaptive level set. J Comput Phys 2007;224: 836–66.

[16] Desjardins O, Blanquart G, Balarac G, Pitsch H. High order conservative finite difference scheme for variable density low Mach number turbulent flows. J Comput Phys 2008;227(15):7125–59.

[17] Kim J, Moin P. Application of a fractional-step method to incompressible Navier–Stokes equations. J Comput Phys 1985;59:308–23.

[18] Pierce C, Moin P. Progress-variable approach for large-eddy simulation of non-premixed turbulent combustion. J Fluid Mech 2004;504:73–97.

[19] Cook AW, Riley JJ. A subgrid model for equilibrium chemistry in turbulent flows. Phys Fluids 1994;6:2868–70.

[20] Balarac G, Raman V, Pitsch H. Development of a consistent dynamic procedure for modeling sub-filter variance. CTR Annual Research Briefs; 2007.

[21] Pierce CD, Moin P. A dynamic model for subgrid-scale variance and dissipation rate of a conserved scalar. Phys Fluids 1998;10:3041–4.

[22] Wall C, Boersma B, Moin P. An evaluation of the assumed beta probability density function subgrid-scale model for large eddy simulation of non-premixed, turbulent combustion with heat release. Phys Fluids 2000;12: 2522–9.

[23] Moreau A, Teytaud O, Bertoglio JP. Optimal estimation for large-eddy simulation of turbulence and application to the analysis of subgrid models. Phys Fluids 2006;18:1–10.

[24] Bedford KW, Yeo WK. Conjective filtering procedures in surface water flow and transport. In: Galperin B, Orszag SA, editors. Large eddy simulation of complex engineering and geophysical flows. New York: Cambridge University Press; 1993.

[25] Clark RA, Ferziger JH, Reynolds WC. Evaluation of subgrid-scale models using an accurately simulated turbulent flow. J Fluid Mech 1979;91:1–16.

[26] da Silva CB, Pereira JCF. Analysis of the gradient-diffusion hypothesis in large-eddy simulations based on transport equations. Phys Fluids 2007;19:1–20.

[27] Lilly D. A proposed modification of the Germano subgrid-scale closure method. Phys Fluids A 1992;4:633–5.

[28] Meneveau C, Lund T, Cabot W. A Lagrangian dynamic subgrid-scale model of turbulence. J Fluid Mech 1996;319:353–85.

[29] Borue V, Orszag S. Local energy flux and subgrid-scale statistics in three-dimensional turbulence. J Fluid Mech 1998;366:1–31.

[30] Liu S, Meneveau C, Katz J. On the properties of similarity subgrid-scale models as deduced from measurements in a turbulent jet. J Fluid Mech 1994;275:83–119.

[31] Mongia H. Recent advances in the development of combustor design tools. In: 39th AIAA/ASME/SAE/ASEE joint propulsion conference and exhibit, No. 4495 in AIAA-2003, Huntsville, AB, USA; July 2003.

[32] Kim W-W, Syed S. Large-eddy simulation needs for gas turbine combustor design. In: 42nd AIAA aerospace sciences meeting and exhibit, No. 331 in AIAA-2004, Reno, NV, USA; January 2004.

[33] Moin P, Apte SV. Large-eddy simulation of realistic gas turbine combustors. AIAA J 2006;44(4):698–708.

[34] Peters N. Private communication; 2006.

[35] Pratt & Whitney and General Electric Aircraft Engines, Critical propulsion components, combustor, vol. 2. NASA/CR-2005-213584/VOL2, NASA; 2005.